Towards quantitative quasi-static elastography with a gravity-induced deformation source

Rebekah H. Griesenauer,[a] Jared A. Weis,[a] Lori R. Arlinghaus,[b] Ingrid M. Meszoely,[c,] Michael I. Miga[a,b,d,e,f*]

[a]Department of Biomedical Engineering, Vanderbilt University, Nashville TN
[b] Vanderbilt University Institute of Imaging Science (VUIIS), Vanderbilt University Medical Center, Nashville TN
[c]Department of Surgery, Vanderbilt University Medical Center, Nashville TN
[d]Vanderbilt Institute in Surgery and Engineering, Vanderbilt University, Nashville TN
[e]Department of Radiology and Radiological Sciences, Vanderbilt University Medical Center, Nashville TN
[f]Department of Neurological Surgery, Vanderbilt University Medical Center, Nashville TN

Abstract. Biomechanical breast models have been employed for applications in image registration and analysis, breast augmentation simulation, and for surgical and biopsy guidance. Accurate applications of stress-strain relationships of tissue within the breast can improve the accuracy of biomechanical models that attempt to simulate breast movements. Reported stiffness values for adipose, glandular, and cancerous tissue types vary greatly. Variations in reported stiffness properties are mainly due to differences in testing methodologies and assumptions, measurement errors, and natural inter patient differences in tissue elasticity. Therefore, patient specific, *in vivo* determination of breast tissue properties is ideal for these procedural applications. Many *in vivo* elastography methods are not quantitative and/or do not measure material properties under deformation conditions that are representative of the procedure being simulated in the model. In this study, we developed an elasticity estimation method that is performed using deformations representative of supine therapeutic procedures. Reconstruction of material properties was performed by iteratively fitting two anatomical images before and after tissue stimulation. The method proposed is work flow friendly, quantitative, and uses a non-contact, gravity-induced deformation source. We tested this material property optimization procedure in a healthy volunteer and in simulation. In simulation, we show that the algorithm can reconstruct properties with errors below 1% for adipose and 5.6% for glandular tissue regardless of the starting stiffness values used as initial guesses. In clinical data, reconstruction errors are higher (3.6% and 24.2%) due to increased noise in the system. In a clinical context, the elastography method was shown to be promising for use in biomechanical model assisted supine procedures.

Keywords: elastography, MRI, lumpectomy, image guidance, biomechanical modeling, registration, breast cancer

***** E-mail: michael.i.miga@vanderbilt.edu

1 Introduction

Breast cancer imaging modalities include x-ray mammography, ultrasound, and magnetic resonance imaging (MRI). In each modality, unique patient positioning confounds the use of diagnostic images for surgical guidance. In x-ray mammography, the patient stands erect with the breasts compressed between two plates. During ultrasound exams, the patient is positioned supine with the ipsilateral arm placed above the patient's head. MRI exams of the breast are typically performed with the patient lying prone with breasts pendant in the MRI coil chambers. During surgery, the patient is positioned supine with the ipsilateral arm placed perpendicular to the body.

Each modality has unique benefits for the screening, diagnosis, and staging of breast cancer. However, there is limited utility in the use of diagnostic images for localizing tumors during surgery. For breast conserving therapy (BCT), which consists of a lumpectomy (removal of tumor and small amount of surrounding healthy tissue) followed by radiation therapy, localization of the tumor during surgery can be difficult. Reoperations due to the presence of residual tumor after an initial resection average 20-40% [1]. Furthermore, ductal carcinoma in situ (DCIS) is associated with a 3-fold increase in reoperation rates when compared to invasive carcinomas [2]. DCIS lesions have diffuse growth patterns and ill-defined margins when compared to invasive breast cancers [3]. Furthermore, DCIS extensions into intraductal tissue can be difficult to determine. Due to the mainstream usage of screening mammography, an increasing number of patients are being diagnosed with DCIS and early stage cancers. Therefore, precise strategies to localize the non-palpable DCIS lesions are needed. While intraoperative ultrasound has been shown to reduce the need for re-excisions [4], ultrasound cannot image most cases of ductal carcinoma in situ (DCIS) and is limited in detecting multifocal disease, bilateral breast cancers, and intraductal spread characteristics [5].

While MRI is considered the most sensitive and accurate imaging modality in the context of breast cancer [6], [7], the limited specificity of MRI provides some areas of improvement. There is some evidence that preoperative MRI causes over treatment and is associated with an increase in the use of mastectomy, delay in treatment, and an increase in the number of additional biopsies [8]–[10]. Alternatively, several studies have disputed these claims arguing that MRI provides invaluable information regarding the extent of disease. In a recent prospective, randomized, multicenter study, a significant decrease in reoperation rates was reported between women who received a preoperative staging MRI vs. women who did not receive an MRI prior to lumpectomy [11]. Sung

et al. published a retrospective analysis that concluded that reoperation rates among BCT patients were lower for women who received a preoperative MRI [12]. Several other studies report positive findings for improved preoperative staging using MRI [11]–[14]. Overall, the argument surrounding the value of preoperative MRI remains somewhat unclear. However, it is generally agreed upon that MRI provides the most accurate delineation of the size and extent of cancer and offers the highest sensitivity for intraductal extension involved in breast cancers [15]–[17].

Regardless, these diagnostic MR images are not particularly useful in the context of surgical planning and guidance. As previously discussed, preoperative MR images are acquired in the prone position with pendant breasts while surgery is performed with the patient lying supine. Several studies have reported significant displacements in breast tumors between the prone and supine positions on the order 18-60 mm [18]–[20]. These relatively large displacements render diagnostic images sub-optimal for use in surgical planning and navigation, which may contribute to studies finding little to no benefit of preoperative MRI for surgical use. Due to these realizations, several groups have investigated the use of preoperative MR images rendered in positions that more closely represent the surgical orientation. Prone-to-supine registration methods of MR images for use in guiding breast surgery have been developed [21], [22]. A more direct approach is to use MR images taken in the supine position to guide surgery. Supine breast imaging has been a topic of interest in several studies [23]–[25]. Furthermore, the use of supine breast MRI in the context of image guided breast surgery (IGBS) has been suggested in several frameworks [18], [26]–[28]. In the context of IGBS, preoperative supine breast images are registered to the physical space of the operating room to act as patient specific maps to assist surgeons in localizing discrete breast lesions. The patient specific aspect of these systems involves the creation of biomechanical computational models to correct for deformation that naturally occurs between the preoperative

image and surgical space breast geometries. In this study, we developed a method to further optimize the patient specific parameters of IGBS systems. In Figure 1, the basic steps for IGBS is shown. The process begins with preoperative imaging of the breast in the supine position. Anatomical and morphological images are obtained at this step. Pre-processing of these images include segmentation of the breast tissue into adipose, fibroglandular, chest wall muscle, and tumor. From here, a FEM model is created to simulate breast tissue deformation during the intraoperative registration step. In the Intraoperative Registration step, the surface of the breast is digitized by an optical tracking system and a biomechanically assisted nonrigid registration is performed to render the preoperative data into the physical space of the operating room. Once this registration is complete, a guidance display of the co-registered preoperative image data is used to localize tumors and map out surgical plans. The extra step we have added and that will be elaborated upon in this study is during the pre-processing step. Here, we estimate the material properties of the patient's breast tissue to be incorporated into the biomechanical model for improved accuracy. In this study, we tested this material property optimization procedure in a healthy volunteer and in simulation.

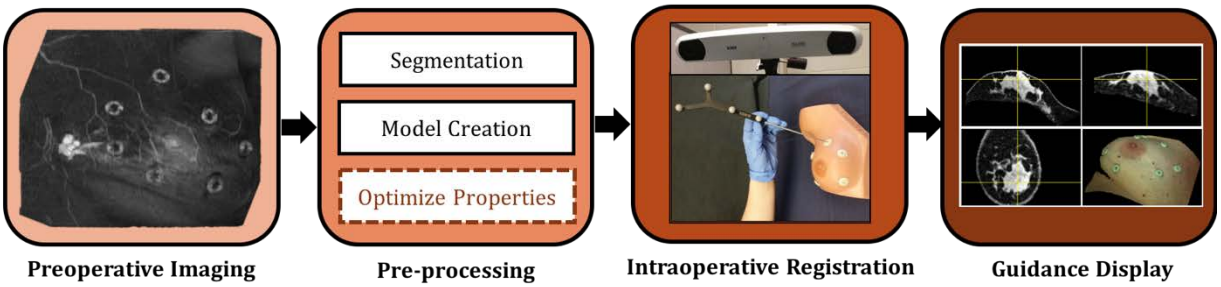

Figure 1 General framework for image-guided breast surgery. The process begins with preoperative imaging of the patient breast in the supine position. The Preoperative Imaging panel shows a representative MR volume rendering of a contrast-enhanced supine breast of a patient with breast cancer. The rendering shows a tumor with elevated image intensity and ring-shaped adhesive surface fiducials used during the Intraoperative Registration step. Pre-processing is performed after imaging, prior to surgery. At this step, patient specific stiffness properties are extracted to optimize the patient specific model. Intraoperative Registration is performed to transform the preoperative image and patient specific model into surgical space. Finally, the Guidance Display is used by the surgical team to localize tumors.

2 Methods

2.1 Overview of Stiffness Estimation Method

Optimization of patient specific breast tissue stiffness beings with acquisition of two gravity-loaded supine breast MR images. The baseline image is acquired with the patient lying supine with the ipsilateral arm placed above her head. Gravity excitation is produced by placing a foam wedge posterior to the breast being imaged. This causes a rotation about the longitudinal axis of the body which results in tissue deformation due to a change in tissue weight distributions with respect to gravity. From the gravity-excited image, an FEM model is created. In this framework, the chest wall is assumed to be a reliably rigid structure and is used to align the baseline and gravity-excited images. The chest wall in each image is segmented and a rigid registration is performed by maximizing the image similarity between the chest walls in each space. The transformation matrix yielded by this chest wall registration is used to transform the baseline image into the gravity-excited space. Now, the chest walls in each space are aligned and the resulting misalignment of the breast tissue is due to the nonrigid deformation caused by differences in gravitational loading. Also from the chest wall alignment, the differences in gravitational loading are quantified by using the rotational component of the transformation matrix to calculate the relative change in the acting gravity direction. The rotated gravity vector is applied as a body force of tissue weight in the biomechanical model. A biomechanical model is then solved to obtain a displacement field. The displacement field is interpolated onto the gravity-excited image to create a model-deformed image. Material properties are iteratively updated until the model-deformed image matches the chest wall-aligned baseline image. A visual representation of this process is shown in Figure 2.

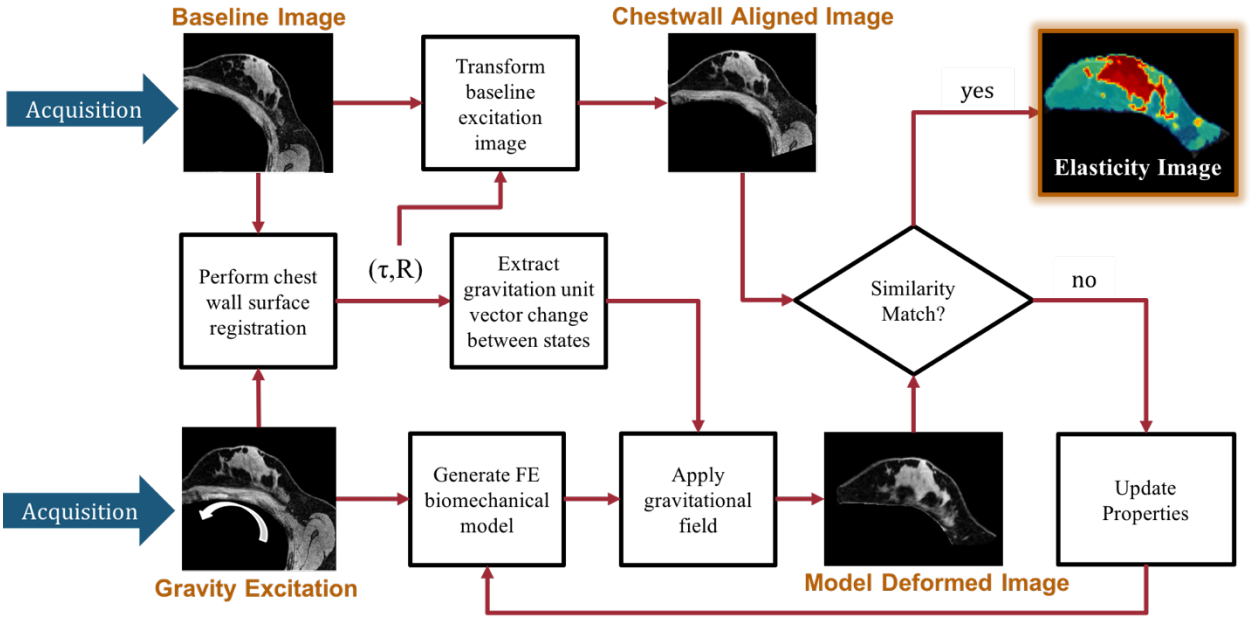

Figure 2 Overview of the process to optimize patient specific material properties. The algorithm estimates tissue elasticity by fitting two acquired anatomical images by minimizing a similarity metric between an experimentally acquired image and a model deformed image.

2.2 Image Acquisition and Biomechanical Model

In an IRB approved study, a 21-year-old healthy female volunteer was enrolled to participate in this study. A baseline and gravity excited image was acquired in a Philips 3T Achieva MR scanner using a SENSE XL Torso Coil (Philips Healthcare, Best, Netherlands) with the following parameters: T_1-weighted, 3D turbo field echo sequence with fat suppression, a field of view of 200 mm × 200 mm × 160 mm, reconstructed voxel size of 0.391 mm × 0.391 mm × 1 mm, TR/TE = 7.422 ms / 3.91 ms, and flip angle = 20 degrees using SENSE parallel imaging (acceleration factor=2).

A FEM tetrahedral mesh was created from the gravity excited image (edge length = 3 mm). The difference in gravitational loading was approximated by calculating a gravity vector: $g_{rotated} = g_{unrotated} - R * g_{unrotated}$, where $g_{unrotated}$ was assumed to be unit vector normal to the MR table and

R is the rotation matrix generated from the rigid chest wall alignment registration. A body force of tissue weight, [9.8m/s^2 × $g_{rotated}$ × ρ], was applied in a biomechanical model that assumes isotropic and Hookean linear elastic behavior. Tissue density, ρ, was estimated as 1000 kg/m^3. Nodal positions corresponding to the chest wall were prescribed a fixed Dirichlet boundary condition with the assumption that the chest wall remains static between the two configurations. Using these parameters, a forward biomechanical model with an FEM corrotational formulation [29] is solved to obtain a displacement field. The displacement field is used to deformed the gravity-excited image. An optimization procedure iteratively updates the stiffness properties of the breast tissue until the model-deformed image matches the baseline image. Optimization of the stiffness parameters were performed using a trust-region-reflective least squares algorithm [30] implemented using the MATLAB R2015 (The Mathworks Inc., Natick, MA) lsqnonlin function.

2.4 Simulation Study

A simulation study was performed to assess the performance of the method with minimal noise contributions and to determine a representative true form of the objective function using similar clinical parameters. Model parameters were selected to form a representative simulated clinical dataset. These parameters include: 500 and 2000 kPa for the stiffness of adipose and glandular tissue, respectively, a Poisson's ratio of 0.45, tissue density of 1000 kg/m^3, and a rotation relative to the initial direction of gravity ($g_{rotated}$) of 15 degrees. Using these parameters, a forward model was solved and the resulting displacement field was interpolated onto the baseline image to create a simulated gravity-excited image. Figure 3 shows representative baseline and simulation images and the corresponding deformation that drives the stiffness estimation procedure.

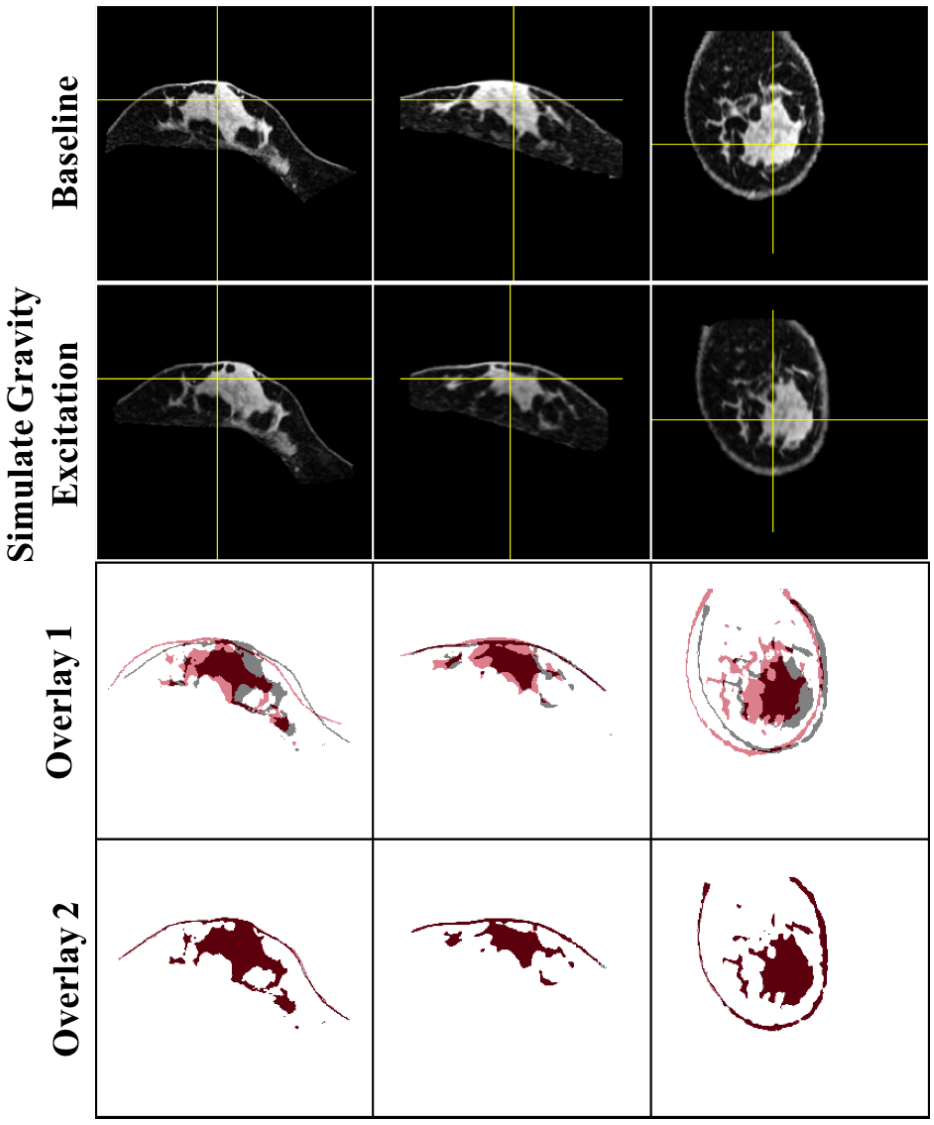

Figure 3 Representative images used in simulation study. The top row contains axial, sagittal, and coronal views of a baseline image. The middle row shows the same three orthogonal slices of the simulated gravity-induced configuration image. The third row (overlay 1) displays the simulated gravity-induced image as a red mask and baseline image as a gray mask. The fourth row (overlay 2) displays the simulated gravity-induced configuration and model deformed image using optimized reconstructed properties. Overlay 1 demonstrates the type of deformation yielded from the gravity induced excitation used in this method.

2.5 Parameter Sweep

To observe material property optimization performance, a parameter sweep was first performed on a moderate search space to obtain an objective function map. The objective function was calculated based on an image similarity metric, S=1-CC, where CC is the image correlation

coefficient. The correlation coefficient takes a value of 1 if the two images are the same and a value of zero if the two images are completely uncorrelated. The root mean squared (RMS) nodal displacement error was also calculated during the simulation parameter sweep. The RMS nodal displacement errors were not available during the *in vivo* human subject parameter sweep because the known correspondence of tissue features is ambiguous. The search space for the parameter sweeps was 100-800 Pa for adipose tissue and 1000-4000 Pa for glandular tissue. The step size for each tissue type was 50 Pa.

2.6 Optimization and Sensitivity to Initial Guess

After the parameter sweep was performed, an estimation of the true minimum was obtained. The sensitivity of the material property optimization to initial guess was then studied using a range of initial guesses for the optimization procedure. The initial guesses were distributed around the minimum obtained during the parameter sweep of the human subject data and the ground truth values for the simulation data.

3 Results

3.1 Parameter Sweep

The parameter sweep in the human study yielded a minimum at 350 Pa (adipose) and 1650 Pa (glandular). The similarity metrics (objective function) maps were of similar shape for the simulation study and the clinical data. The nodal displacement error map, shown in Figure 4, also shows an elongated minimum in the glandular direction. This shallow gradient in the glandular direction contributes to errors in the optimization step.

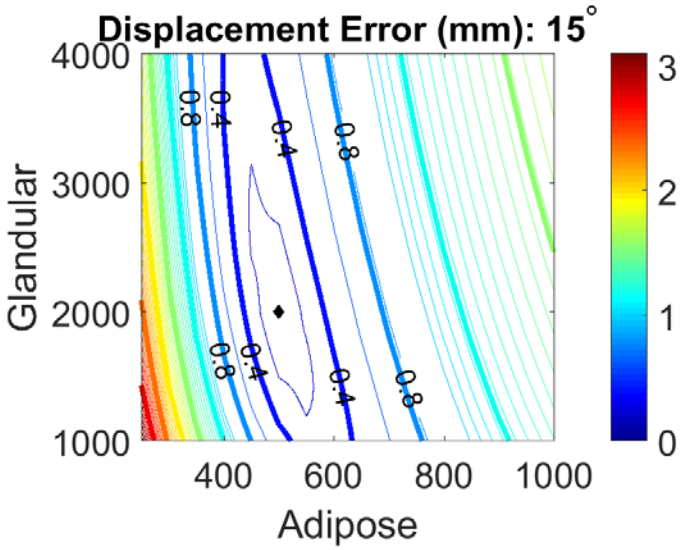

Figure 4 RMS nodal displacement errors for simulation parameter sweep. The x-axis contains the range of stiffness values sampled for adipose tissue. The y-axis is the range of stiffness values sampled for glandular tissue. The contour levels represent the nodal displacement error at that adipose-glandular combination. The contour map also shows the 0.4 mm and 0.8 mm contour levels which roughly corresponds to the half and full voxel sizes of the image volumes used in this study. The diamond shows the location of the minimum displacement error (i.e. the true properties)

3.2 Optimization and Sensitivity to Initial Guess

The average percent error for the simulation data was 0.9% for adipose tissue and 5.6% for glandular tissue. The average percent error for the clinical data was 3.6% for adipose tissue and 24.2% for glandular tissue. The percent error for adipose tissue was significantly lower than the percent error for glandular tissue. The reason for this can be seen in the objective function map where contours in the glandular direction were shallow when compared to the steep gradients in the adipose directions. Starting values of glandular tissue had the most influence on the optimization results, with lower starting values for glandular tissue resulting in the optimization landing on a local minimum. In simulation, reconstructed stiffness properties converged at the global minimum despite initial guess. In clinical data, noise is introduced into the system, resulting in convergence of material properties into local minimums.

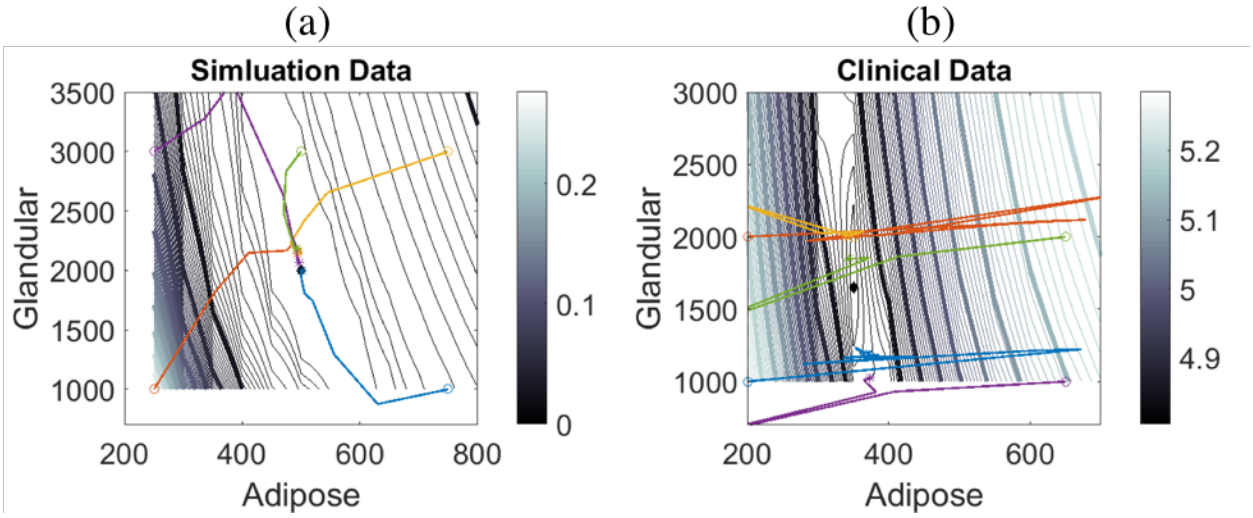

Figure 5 Parameter sweep and optimization results from simulation data (a) and clinical data (b). Image similarity objective function maps are shown for (a) simulation data and (b) clinical data. The grayscale contour levels represent the image similarity error at each adipose-glandular combination sampled in the parameter sweep. Plots of optimization results are overlaid onto the image similarity maps. Each colored line represents an optimization run with different starting values for adipose and glandular tissue. Circles indicate starting points while asterisks indicate optimization minimums.

4 Discussion

We developed a framework to optimize material properties of breast tissue in an effort to incorporate patient specific parameters for an image guided breast surgery system. In simulation, we show that the algorithm can reconstruct properties with errors below 1% for adipose and 5.6% for glandular tissue regardless of the starting stiffness values used as initial guesses. In clinical data, reconstruction errors are higher (3.6% and 24.2%) due to increased noise in the system. These errors are within an acceptable range as they introduce to less than 0.4 mm errors into the system. This can be seen from Figure 4 where displacement errors between 1500 to 2500 Pa for glandular (+/- 25% of true glandular value) and 480 and 520 Pa for adipose (+/- 4% of true values) lie below the 0.4 mm contour level. The behavior we see is intriguing and questions remain. For example, in patients with higher glandular content, does the concentricity and sharpness of the functional space change dramatically? Or with gravity-based excitation, are there limitations that prevent reconstruction or for that matter, enhance reconstruction? These types of question will be looked

at in the future. Nevertheless, this work provides encouragement to pursue the testing of this framework in a larger human study and provides a step forward in the patient specific models created to improve tumor localization for breast cancer surgeries.

Disclosures

The authors disclose no conflicts of interest.

Acknowledgments

The authors would like to acknowledge the support of the National Institutes of Health through K25CA204599, R21EB022380 and the National Science Foundation for a Graduate Research Fellowship awarded to R.H.G.

References

[1] J. Landercasper, E. Whitacre, A. C. Degnim, and M. Al-Hamadani, "Reasons for re-excision after lumpectomy for breast cancer: insight from the american society of breast surgeons masterysm database," *Ann. Surg. Oncol.*, vol. 21, no. 10, pp. 3185–3191, 2014.

[2] L. Langhans, M.-B. Jensen, M.-L. M. Talman, I. Vejborg, N. Kroman, and T. F. Tvedskov, "Reoperation Rates in Ductal Carcinoma In Situ vs Invasive Breast Cancer After Wire-Guided Breast-Conserving Surgery," *JAMA Surg.*, 2016.

[3] K. A. Skinner, H. Silberman, R. Sposto, and M. J. Silverstein, "Palpable Breast Cancers Are Inherently Different From Nonpalpable Breast Cancers," *Ann. Surg. Oncol.*, vol. 8, no. 9, pp. 705–710, 2001.

[4] N. M. A. Krekel *et al.*, "Intraoperative ultrasound guidance for palpable breast cancer excision (COBALT trial): a multicentre, randomised controlled trial," *Lancet Oncol.*, vol. 14, no. 1, pp. 48–54, 2013.

[5] C. H. Lee *et al.*, “Breast cancer screening with imaging: recommendations from the Society of Breast Imaging and the ACR on the use of mammography, breast MRI, breast ultrasound, and other technologies for the detection of clinically occult breast cancer,” *J. Am. Coll. Radiol.*, vol. 7, no. 1, pp. 18–27, 2010.

[6] C. K. Kuhl *et al.*, “Mammography, breast ultrasound, and magnetic resonance imaging for surveillance of women at high familial risk for breast cancer,” *J. Clin. Oncol.*, vol. 23, no. 33, pp. 8469–8476, 2005.

[7] M. S. Group, “Screening with magnetic resonance imaging and mammography of a UK population at high familial risk of breast cancer: a prospective multicentre cohort study (MARIBS),” *Lancet*, vol. 365, no. 9473, pp. 1769–1778, 2005.

[8] L. Turnbull *et al.*, “Comparative effectiveness of MRI in breast cancer (COMICE) trial: a randomised controlled trial,” *Lancet*, vol. 375, no. 9714, pp. 563–571, 2010.

[9] C. Kuhl, W. Kuhn, M. Braun, and H. Schild, “Pre-operative staging of breast cancer with breast MRI: one step forward, two steps back?,” *The breast*, vol. 16, pp. 34–44, 2007.

[10] N. Houssami *et al.*, “Accuracy and surgical impact of magnetic resonance imaging in breast cancer staging: systematic review and meta-analysis in detection of multifocal and multicentric cancer,” *J. Clin. Oncol.*, vol. 26, no. 19, pp. 3248–3258, 2008.

[11] V. Gonzalez *et al.*, “Preoperative MRI of the breast (POMB) influences primary treatment in breast cancer: a prospective, randomized, multicenter study,” *World J. Surg.*, vol. 38, no. 7, pp. 1685–1693, 2014.

[12] J. S. Sung *et al.*, “Preoperative breast MRI for early-stage breast cancer: effect on surgical and long-term outcomes,” *Am. J. Roentgenol.*, vol. 202, no. 6, pp. 1376–1382, 2014.

[13] L. Esserman, N. Hylton, L. Yassa, J. Barclay, S. Frankel, and E. Sickles, “Utility of

magnetic resonance imaging in the management of breast cancer: evidence for improved preoperative staging," *J. Clin. Oncol.*, vol. 17, no. 1, p. 110, 1999.

[14] U. Fischer, O. Zachariae, F. Baum, D. von Heyden, M. Funke, and T. Liersch, "The influence of preoperative MRI of the breasts on recurrence rate in patients with breast cancer," *Eur. Radiol.*, vol. 14, no. 10, pp. 1725–1731, 2004.

[15] C. K. Kuhl *et al.*, "MRI for diagnosis of pure ductal carcinoma in situ: a prospective observational study," *Lancet*, vol. 370, no. 9586, pp. 485–492, 2007.

[16] M. D. Pickles, P. Gibbs, A. Hubbard, A. Rahman, J. Wieczorek, and L. W. Turnbull, "Comparison of 3.0 T magnetic resonance imaging and X-ray mammography in the measurement of ductal carcinoma in situ: A comparison with histopathology," *Eur. J. Radiol.*, vol. 84, no. 4, pp. 603–610, 2015.

[17] J. A. Pain, S. R. Ebbs, R. P. Hern, S. Lowe, and J. W. Bradbeer, "Assessment of breast cancer size: a comparison of methods.," *Eur. J. Surg. Oncol. J. Eur. Soc. Surg. Oncol. Br. Assoc. Surg. Oncol.*, vol. 18, no. 1, pp. 44–48, 1992.

[18] M. J. Pallone, S. P. Poplack, H. B. R. Avutu, K. D. Paulsen, and R. J. Barth, "Supine breast MRI and 3D optical scanning: A novel approach to improve tumor localization for breast conserving surgery," *Ann. Surg. Oncol.*, vol. 21, no. 7, pp. 2203–2208, 2014.

[19] H. Satake, S. Ishigaki, M. Kitano, and S. Naganawa, "Prediction of prone-to-supine tumor displacement in the breast using patient position change: investigation with prone MRI and supine CT," *Breast Cancer*, vol. 23, no. 1, pp. 149–158, 2016.

[20] L. A. Carbonaro, P. Tannaphai, R. M. Trimboli, N. Verardi, M. P. Fedeli, and F. Sardanelli, "Contrast enhanced breast MRI: spatial displacement from prone to supine patient's position. Preliminary results," *Eur. J. Radiol.*, vol. 81, no. 6, pp. e771–e774,

2012.

[21] L. Han *et al.*, “A nonlinear biomechanical model based registration method for aligning prone and supine MR breast images,” *IEEE Trans. Med. Imaging*, vol. 33, no. 3, pp. 682–694, 2014.

[22] L. Han *et al.*, “A hybrid fem-based method for aligning prone and supine images for image guided breast surgery,” in *Biomedical Imaging: From Nano to Macro, 2011 IEEE International Symposium on*, 2011, pp. 1239–1242.

[23] P. Siegler, C. Holloway, P. Causer, G. Thevathasan, and D. B. Plewes, “Supine breast MRI,” *J. Magn. Reson. Imaging*, vol. 34, no. 5, pp. 1212–1217, 2011.

[24] T. H. Kim, D. K. Kang, and Y. S. Jung, “MR-navigated ultrasound with supine breast MRI for suspicious enhancing lesions not identified on second-look ultrasound in breast cancer patients,” *Ultraschall der Medizin-European J. Ultrasound*, vol. 37, no. S 01, p. SL16_3, 2016.

[25] D. K. Kang, Y. Jung, S. Han, J. Y. Kim, and T. H. Kim, “Clinical Utility of Real-Time MR-Navigated Ultrasound with Supine Breast MRI for Suspicious Enhancing Lesions Not Identified on Second-Look Ultrasound,” *Ultrasound Med. Biol.*, vol. 43, no. 2, pp. 412–420, 2017.

[26] R. H. Conley *et al.*, “Realization of a biomechanical model-assisted image guidance system for breast cancer surgery using supine MRI,” *Int. J. Comput. Assist. Radiol. Surg.*, vol. 10, no. 12, pp. 1985–1996, 2015.

[27] R. H. Conley, I. M. Meszoely, T. S. Pheiffer, J. A. Weis, T. E. Yankeelov, and M. I. Miga, “Image to physical space registration of supine breast mri for image guided breast surgery,” in *SPIE medical imaging*, 2014, p. 90362N–90362N.

[28] T. Alderliesten *et al.*, “On the feasibility of MRI-guided navigation to demarcate breast cancer for breast-conserving surgery,” *Med. Phys.*, vol. 37, no. 6, pp. 2617–2626, 2010.

[29] G. F. Moita and M. A. Crisfield, “A finite element formulation for 3-D continua using the co-rotational technique,” *Int. J. Numer. Methods Eng.*, vol. 39, no. 22, pp. 3775–3792, 1996.

[30] M. A. Branch, T. F. Coleman, and Y. Li, “A subspace, interior, and conjugate gradient method for large-scale bound-constrained minimization problems,” *SIAM J. Sci. Comput.*, vol. 21, no. 1, pp. 1–23, 1999.